PAPER

Comparing interatomic potentials in calculating basic structural parameters and Peierls stress in tungsten-based random binary alloys

Physica Scripta

PAPER

Comparing interatomic potentials in calculating basic structural parameters and Peierls stress in tungsten-based random binary alloys

RECEIVED
25 May 2023

REVISED
28 July 2023

ACCEPTED FOR PUBLICATION
30 August 2023

PUBLISHED
11 September 2023

Abdullah Al Mamun[1], **Shuozhi Xu**[2], **Xiang-Guo Li**[3] and **Yanqing Su**[1]

[1] Department of Mechanical and Aerospace Engineering, Utah State University, Logan, UT 84322-4130, United States of America
[2] School of Aerospace and Mechanical Engineering, University of Oklahoma, Norman, OK 73019-1052, United States of America
[3] School of Materials, Shenzhen Campus of Sun Yat-sen University, No. 66, Gongchang Road, Guangming District, Shenzhen, Guangdong 518107, People's Republic of China

E-mail: yanqing.su@usu.edu

Keywords: binary alloys, Peierls stress, machine learning-based interatomic potentials, basic structural parameters

Abstract

The field of machine learning-based interatomic potentials (ML-IAPs) has seen increasing development in recent years. In this work, we compare three widely used ML-IAPs–the moment tensor potential (MTP), the spectral neighbor analysis potential (SNAP), and the tabulated Gaussian approximation potential (tabGAP)with a conventional non-ML-IAP, the embedded atom method (EAM) potential. We evaluated these potentials on the basis of their accuracy and efficiency in determining basic structural parameters and Peierls stress under equivalent conditions. Three tungsten (W)-based alloys (Mo-W, Nb-W, and Ta-W) are considered, and their lattice parameter, formation energy, elastic tensor, and Peierls stress of edge dislocation are calculated. Compared with DFT results, MTP demonstrates the highest accuracy in predicting the lattice parameter and the best computational efficiency among the three ML-IAPs, while tabGAP accurately predicts two independent elastic constants, C_{11} and C_{12}. Despite being the slowest, SNAP shows the highest accuracy in predicting the third independent elastic constant C_{44} and its Peierls stress value is comparable to that based on MTP.

1. Introduction

Binary alloys are promising structural materials. For example, the equal molar titanium-zirconium alloy possesses approximately 2.5 times hardness and tensile strength compared with pure titanium and pure zirconium and is being used in biomedical materials [1]. Alloying tungsten with rhenium solves the tungsten's low ductility issue and increases its toughness in the meanwhile [2]. Binary transition metal-alloyed nanoparticles are becoming more popular, as their application ranges from (electro-)catalysis to biomedical devices, owing to their good bio-compatibility, easy size control, high performance, and low cost [3]. Recently, biodegradable zinc-copper alloys were developed for cardiovascular implant [4]. Investigating binary alloys is also considered as one preliminary step for developing multi-principal element alloys (MPEAs), which consist of three or more principal metallic elements [5–7]. MPEAs are drawing growing attention because of their enhanced properties in extreme environments [8]. For example, face-centered cubic (fcc) MPEAs have shown high damage tolerance and strength at cryogenic temperatures [9, 10], while body-centered cubic (bcc) MPEAs possess high melting points and exceptional mechanical strength at elevated temperatures [11, 12]. Due to the infinite possibility of compositions and their ratios, predicting the properties of MPEAs is difficult [13, 14]. So it is useful to first study binary systems to obtain the characteristic traits of constituent elements and their combinations [15].

In the past century, binary alloy systems have been characterized experimentally [16]. Most research was done on Ni-based and Fe-based alloys [17–21]. For transition metal alloys from groups V and VI, most studies

concerned the mechanical and thermodynamic properties of ternary or quaternary alloy systems [12, 22–25]. There is a significant knowledge gap for random binary alloys comprising group V and VI metals.

Among those metals, tungsten (W) has the highest melting point and excellent thermal conductivity and thus serves in the high heat flux environment [26]. In addition, W attains good sputtering resistance and low tritium retention, making it a promising candidate for the plasma-facing material in fusion reactor diverters [27]. In the meantime, W has some shortcomings such as a high ductility-to-brittle transition temperature and a high tendency for embrittlement subject to neutron irradiation [28, 29]. To address these issues, several modification techniques were used and alloying is one of them [30]. In alloying W, two key questions are: (i) 'what is the alloying metal?' and (ii) 'how much alloying metal should be added to W?'. The goal is to improve, and preferably, maximize the strength of W-based random binaries. In these alloys, plastic deformation and strengthening are fundamentally controlled by dislocation gliding, which requires a minimum resolved shear stress called the Peierls stress.

In this study, we will address how alloying metals, such as Mo, Nb, and Ta, with given atomic percentages, change the basic structural parameters and Peierls stress compared with pure W. The structural parameters, including lattice parameters and elastic constants, and Peierls stress of dislocation at the atomic scale can be calculated using either the molecular static (MS) method or density functional theory (DFT), using simulation tools such as LAMMPS [31] and VASP [32], respectively. DFT calculations depend on quantum mechanical descriptions for the potential energy surface (PES) which has the highest accuracy and best transferability [33]. However, it is limited to systems containing ~100–1000 atoms due to the high computational cost, making DFT unsuitable for large-scale simulations [34, 35]. In the meantime, MS simulations can be employed to study systems containing millions or even billions of atoms; however, their accuracy significantly depends on the interatomic potentials (IAPs) [36, 37]. For metallic alloys, embedded-atom method (EAM) potential [38] and its derivative (e.g., modified EAM [39] were previously considered state-of-the-art. They showed great predictive capabilities for metals. At first, EAM potentials for most metallic elements were developed by fitting to DFT or experimental data [40]; then potentials for alloy systems like binary, ternary, quaternary, and MPEAs were gradually developed [41].

Recently, numerous machine learning-based IAPs (ML-IAPs) emerged for a variety of metals and alloys [42]. It was first introduced in 1995 by Blank *et al* [43], who modeled a neural network system for predicting the PES. Later, in 2010, Bartok *et al* [44] presented the Gaussian approximation potential (GAP) for diamond. GAP doesn't have any fixed functional form, hence capable of modeling complex potential energy landscapes. Then, in 2015, the spectral neighbor analysis potential (SNAP) was introduced by Thompson *et al* [45]. SNAP describes the local environment of each atom by a set of bispectrum components of the local neighbor density projected onto a basis of 4D hyperspherical harmonics. In 2016, Shapeev [46] introduced the moment tensor potential (MTP). SNAPs have been employed to calculate basic structural parameters and Peierls stress in several pure bcc metals (including W) [47], showing that they perform better than EAM potential, with respect to DFT data.

In this paper, we are extending that piece of work to several ML-IAPs and comparing their performance in several W-based random binary alloys. Three ML-IAPs are considered: SNAP, MTP, and tabulated GAP (tab-GAP). EAM potentials are also included for comparative analysis. All four potentials are applied to obtaining basic structural parameters and Peierls stress of edge dislocation in three sets of random binary alloys: $Mo_{1-x}W_x$, $Nb_{1-x}W_x$, and $Ta_{1-x}W_x$, with x varying from 0 to 1, in increments of 0.1. To quantify the performance of these ML-IAPs, DFT and experimental values [48] are presented and compared with our results, whenever possible. This study does not aim to conclusively evaluate the quality or accuracy of the potentials based solely on these comparisons. The primary objective is to present the data, allowing readers to form their own interpretations in the context of their specific needs and objectives.

2. Methodology

2.1. Interatomic potentials

In this study, we use one EAM potential and three ML-IAPs. The EAM potential is the one developed for the CrMoNbTaVW system [15]. The ML-IAPs include SNAP, originally developed for NbMoTaW [8], a tabulated GAP, for MoNbTaVW [49], and MTP, for MoNbTaW [50]. In all these IAPs, the force on an atom F_i is the derivative of the total potential energy E_{tot} with respect to its position r_i, i.e.,

$$F_i = \frac{\partial E_{\text{tot}}}{\partial r_i} \tag{1}$$

EAM potential. In EAM formulation, the potential energy of an atom i is a sum of two terms: an embedding potential and a pair potential [51], i.e.,

$$E_i = P_i\left(\sum_{j\neq i}\rho_j(r_{ij})\right) + \frac{1}{2}\sum_{j\neq i}\phi_{ij}(r_{ij}) \tag{2}$$

Here, ρ_j is the contribution to the atomic density from atom j, r_{ij} is the distance between atoms i and j, and ϕ_{ij} is the short-range pair potential [52]. In equation (2), both sums are taken over all neighboring atoms of the atom i. This enables a detailed description of the interactions between atoms while considering their environments [38].

ML-IAPs. In all ML-IAPs, an atom's potential energy is a function of the local environment descriptor. Different ML-IAPs differ in (i) descriptors for the local environment around each atom and (ii) the ML model used to map the descriptors to the PES [53]. Compared with non-ML-IAPs such as the EAM potential, main features of the ML-IAPs include (i) the PES is based on numerical interpolation with respect to DFT data, and (ii) the PES is correlated to local environment descriptors instead of atom position vectors [44, 46, 53].

SNAP. SNAP calculates the potential energy of an atom based on its representation in the spectral space, which is a space where atoms are represented as points based on their positions and interatomic distances [45]. SNAP uses the bispectrum basis to describe the local environment [44]. The atomic energies and forces are a function of the bispectrum coefficients of the atomic neighbor density function. The potential energy and the bispectrum components are usually assumed to have a linear relationship. To establish this relationship, a neural network model is used. Clusters of atoms that are close to one another make up the majority of the energy in an arrangement of atoms [45]. The total potential energy E_{tot} and force f_j on atom j are expressed as a function of k projected bispectrum components B_k, i.e.,

$$E_{\text{tot}} = \sum_{\alpha}\left(\beta_{\alpha,0}N_\alpha + \sum_{k=1}^{K}\beta_{\alpha,k}\sum_{i=1}^{N_\alpha}B_{k,i}\right) \tag{3}$$

$$\mathbf{f}_j = -\sum_{\alpha}\sum_{k=1}^{K}\beta_{\alpha,k}\sum_{i=1}^{N_\alpha}\frac{\partial B_{k,i}}{\partial \mathbf{r}_j} \tag{4}$$

where α is the atomic type, N_α is the total number of type α atoms, k is the neighboring site of type α atoms, K is the total number of neighboring sites. SNAP uses coefficients denoted as $\beta_{\alpha,k}$ in its linear equation to model the activation energies for type α atoms. The distribution of neighboring atoms surrounding atom i at position $\mathbf{r}$ can be expressed as a summation of δ-functions located within a three-dimensional spatial domain. The atomic neighbor density function can be expressed as [8]

$$\rho_i = \delta(\mathbf{r}) + \sum_{r_{ik}<R_c} f_c(r_{ik})S^k_{\text{atom}}\delta(\mathbf{r}-\mathbf{r}_{ik}) \tag{5}$$

where $\delta(\mathbf{r}-\mathbf{r}_{ik})$ is the Dirac delta function with its center at each neighboring site k. To make the neighbor atomic density zero at the cutoff radius R_c, a cutoff function f_c is employed. S^k_{atom} differs for different atom types. The atomic density function can be represented using a generalized Fourier series expressed in four-dimensional spherical harmonics $U^j_{m,m'}$ as:

$$\rho_i(\mathbf{r}) = \sum_{j=0}^{\infty}\sum_{m,m'=-j}^{j} u^j_{m,m'}U^j_{m,m'} \tag{6}$$

where $u^j_{m,m'}$ are coefficients. The bispectrum coefficients can be expressed as:

$$B_{j_1,j_2,j} = \sum_{m_1,m'_1=-j_1}^{j_1}\sum_{m_2,m'_2=-j_2}^{j_2}\sum_{m,m'=-j}^{j}(u^j_{m,m'})C^{jm}_{j_1m_1j_2m_2}\times C^{jm'}_{j_1m'_1j_2m'_2}u^{j_1}_{m'_1,m_1}u^{j_2}_{m'_2,m_2} \tag{7}$$

where $C^{jm'}_{j_1m'_1j_2m'_2}$ are the coupling coefficients analogous with Clebsch-Gordon coefficients [45]. These coefficients represent the relationship between the activation energy and molecular features for a specific type of atom and are derived from fitting the model to DFT data.

MTP. MTP is based on the idea of interatomic pairwise potential energy moments. MTP builds contracted rotationally invariant local environment descriptors for each atom in the system. These descriptors are then used to create a polynomial regressed correlation between the PES and these descriptors [46]. The potential energy E_i can be expressed as:

$$E_i(\boldsymbol{r}) = \sum_l \beta_l B(\boldsymbol{r}) \tag{8}$$

where $B(\boldsymbol{r})$ are basis functions, each multiplied by a coefficient β_l that is used to describe the local environment of atom i. The basis functions B are derived from the moment tensors and provide a compact representation of the interatomic interactions in the local environment. The moment tensors are also called descriptors and can be expressed as:

Table 1. Summary of different potential fitting processes and basic parameters of training data.

IAP	Fitting parameters	Machine learning technique	Basic parameters for DFT calculations
SNAP [8]	Formation energies, atomic forces	Least square algorithm, differential evolution algorithm	cutoff energy 520 eV, K-point mesh 4 × 4 × 4, supercell size 3 × 3 × 3, energy threshold 10^{-5} eV, force threshold 0.02 eV/Å
tabGAP [55]	Total energies, forces, virial stresses	Gaussian process regression	Cutoff energy 500 eV, max K-point spacing .15/Å, smearing parameter 0.1 eV, supercell size 3 × 3 × 3
MTP [50]	Total energies, atomic forces	Linear regression	cutoff energy 520eV, K-point mesh 4 × 4 × 4, supercell size 3 × 3 × 3, energy threshold 10^{-5} eV, force threshold 0.02 eV/Å
EAM [15]	—	—	Cutoff energy 600 eV, smearing width 0.2 eV, K-point mesh 11 × 11 × 11

$$M_{\mu,\nu}(\boldsymbol{r}) = \sum_j f_\mu(|r_{ij}|, z_i, z_j)\underbrace{\boldsymbol{r}_{ij}\otimes \ldots \otimes \boldsymbol{r}_{ij}}_{\nu \text{ times}} \tag{9}$$

where the functions f_μ represent the radial distribution of the local environment around atom i, and they are specific to the type of neighbor atom j, z_j. The terms $\boldsymbol{r}_{ij} \otimes \ldots \otimes \boldsymbol{r}_{ij}$ are tensors that capture the angular information about the local environment and have a rank of ν. These tensors describe the shape and orientation of the local environment relative to atom i. The functions f_μ and the tensors $\boldsymbol{r}_{ij}\otimes \ldots \otimes \boldsymbol{r}_{ij}$ work together to provide a comprehensive description of the local environment of atom i. The basis functions $B(\boldsymbol{r})$ are created by combining the moment tensors $M_{\mu,\nu}$ into a scalar.

Another two important hyperparameters in MTP are: the cutoff radius r_{cut}, which sets the extent of atomic interactions in the local environment, and maximum level lev_{max} which controls the completeness of basis functions $B(\boldsymbol{r})$. They determine the accuracy, cost of computation, and likelihood of overfitting of MTP [50].

tabGAP. The GAP model uses Gaussian process regression to predict the energy of a material [54]. The prediction is made by combining multiple kernels K using linear weights α_s that are optimized during the regression. An advantage of GAP is that it can use multiple different descriptors at the same time, each represented by a separate term in the prediction, and all of them are trained as a single model. The total energy of a system of atoms can be expressed as a sum of an external repulsive potential E_{rep} and other factors, i.e.,

$$E_{\text{tot}} = E_{\text{rep}} + \sum_d \delta_d^2 \sum_i \sum_s \alpha_s K_d(\boldsymbol{q}_{d,i}, \boldsymbol{q}_{d,s}). \tag{10}$$

where d represents a specific descriptor, and i is used to iterate over all descriptor environments within the system. The summation over s is calculated using sparse Gaussian process regression and is based on a chosen set of descriptor environments from the training data. E_{rep} is the screened Coulomb potential and δ_d^2 is a weighting factor for the descriptor d. The kernel function K_d is used for the descriptor d, and $\boldsymbol{q}_{d,i}$ is the output for the descriptor for the local atomic environment i.

The tabGAP model first uses the GAP framework for training [44]. In GAP, the local environment descriptor is formed from both two-body (2b) and three-body (3b) Gaussian functions of interatomic distances with bond angles multiplied by a smooth cutoff function [42]. The use of low-dimensional descriptors (2b, 3b) in the prediction of GAP energies has several advantages [55]. These descriptors can be efficiently mapped onto discrete grids and interpolated using cubic splines, which is faster than the original Gaussian process regression. The energies from each descriptor are combined using 1D and 3D spline interpolations to create a tabGAP. The total potential energy can be expressed as:

$$E_{\text{tot}} = \sum_{i<j}^{N} S^{\text{1D}}_{\text{rep.}\,+\,\text{2b}}(r_{ij}) + \sum_{i,j<k}^{N} S^{\text{3D}}_{ijk}(r_{ij}, r_{ik}, \cos\theta_{ijk}) \tag{11}$$

where S represents 1D and 3D cubic-spline interpolations. The 3D spline performs interpolation between points on a grid based on the values of $(r_{ij}, r_{ik}, \cos\theta_{ijk})$ [55], where θ_{ijk} is the angle between the interatomic bonds between atoms i, j, and k.

Table 1 provides a summary of all four potentials, which includes the fitting parameters, the applied machine learning techniques, and the essential parameters of DFT-calculated training data along with its validation. Both SNAP and MTP potentials are trained using the same set of training data. The cutoff energy of tabGAP closely mirrors that of MTP and SNAP's training data, exhibiting only a slight difference.

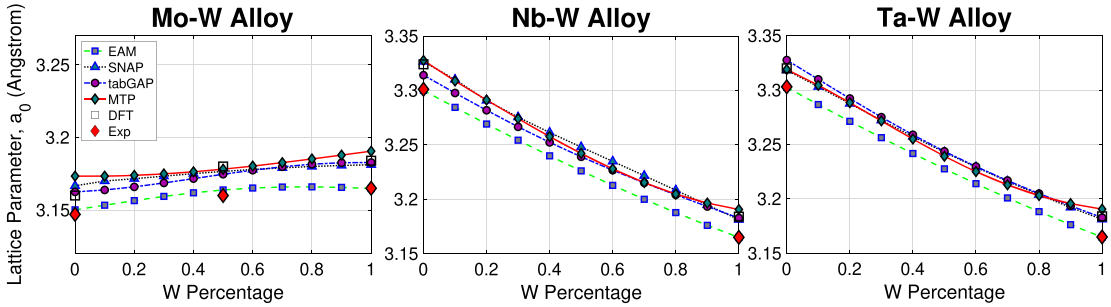

Figure 1. Lattice parameters based on different IAPs in three alloys are plotted with respect to the percentage of W in the alloy. The experimental and DFT data are from [62, 67].

2.2. Molecular static simulations

We used LAMMPS [31] for all MS simulations. For the same type of simulation, the same computational resources are used among different IAPs to compare their computation time. To calculate the basic structural parameters, a cubic simulation cell is built, with all boundaries being periodic. To determine the lattice parameter a_0, we use the 'energy-volume method' [47]. The minimum bulk energy is recorded as E_{bulk}, and a_0 can be derived from the corresponding cell size. From E_{bulk}, we derived the formation energy E_{form} of each binary alloy [56], via

$$E_{\text{form}} = \frac{E_{\text{bulk}} - n_{\text{A}}E_{\text{A}} - n_{\text{B}}E_{\text{B}}}{n_{\text{A}} + n_{\text{B}}} \tag{12}$$

where n_{A} and n_{B} are the number of atoms of elements A and B in the binary compound respectively. E_{A} and E_{B} are the cohesive energy of elements A and B respectively. To calculate the three independent elastic constants C_{11}, C_{12} and C_{44}, we employ the 'stress-strain method' [57]. Based on these three constants, we can obtain important moduli such as bulk modulus and shear modulus.

To calculate the Peierls stress, we use the periodic array of dislocation (PAD) model [58]. The crystallographic orientations are set to be $x[111]$, $y[1\bar{1}0]$, and $z[11\bar{2}]$. Periodic boundary conditions are applied in the x and z directions, while in the y direction, the boundaries are traction-free. An edge dislocation with Burgers vector of $\mathbf{b} = (a_0/2)\langle 111\rangle$ is inserted into the center of the simulation cell. The dislocation line is aligned with the z axis and the x–z plane corresponds to the slip plane, in which the dislocation lies. Scripts to create the PAD models in Nb can be downloaded at https://github.com/shuozhixu/PhysScr_2023.

Each simulation cell begins as a cuboid and transforms into a triclinic shape as the shear strain ϵ_{xy} increases until the maximum strain of 0.12 is attained. The strain increment is set to $|\Delta\epsilon_{xy}| = 2 \times 10^{-5}$ [59]. Energy minimization using the conjugate gradient algorithm and the fast inertial relaxation engine method [60] are conducted following each strain increment. Once the dislocation line moves by at least 1 nm, we record the resolved shear stress and take it as the Peierls stress σ_{p}. Note that all points on the dislocation line move together and the line remains straight during glide. In other words, there is no kink or jog. To visualize the atomic structure and dislocation movement, we used OVITO [61].

3. Results and discussion

3.1. Lattice parameter

Figure 1 shows values of the lattice parameter a_0 predicted by four IAPs. In Mo-W alloys, a_0 increases as the percentage of W increases. The three ML-IAPs used in this study predicted a value of a_0 within 0.4% variation, which is negligible. However, the average difference between the EAM potential and the ML-IAPs is 1.4%. From table 2 with respect to the DFT-based a_0 of the $Mo_{0.5}W_{0.5}$ alloy, the EAM potential, SNAP, tabGAP, and MTP yield error percentages of 0.51%, 0.1%, 0.17%, and 0.06%, respectively. In other words, the MTP produces the smallest error while the EAM potential is the largest [62]. Similarly, for Nb-W alloys, the value of a_0 varies within 0.33% among all ML-IAPs. The difference between the EAM potential and ML-IAPs is 2%. The same trend is also observed for the Ta-W alloys, where the average difference between the EAM potential and ML-IAPs is 1.6%, with a difference of 0.1% among the latter three potentials. We note that in Nb-W and Ta-W alloys, a_0 decreases as the percentage of W increases, in contrary to the trend in Mo-W alloys.

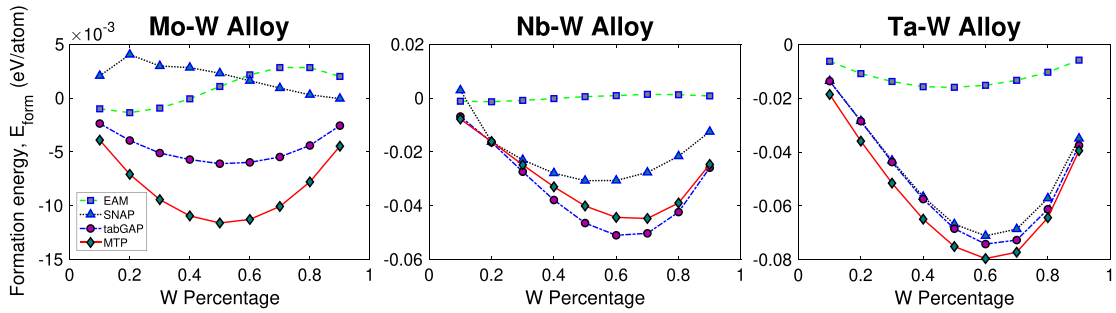

Figure 2. Formation energies based on different IAPs in three alloys are plotted with respect to the percentage of W in the alloy.

Table 2. Basic structural parameters of the $Mo_{0.5}W_{0.5}$ alloy, predicted by the four IAPs, as compared with experimental and DFT data. Error percentage relative to DFT values are shown in parentheses.

	Exp [62]	DFT [62]	EAM	SNAP	tabGAP	MTP
a_0 (Å)	3.16	3.18	3.16 (-0.6%)	3.18(0%)	3.17(0%)	3.18(0%)
C_{11} (GPa)	—	480	493(2.7%)	513(6.8%)	479(0%)	433(−9.8%)
C_{12} (GPa)	—	194	192(-1%)	197(1.5%)	174(-10.3%)	159(−18%)
C_{44} (GPa)	—	117	133(13.7%)	134(14.5%)	95(-18.8%)	99(−15.4%)
B_{mod} (GPa)	—	289	292(1%)	302(4.5%)	276(-4.5%)	250(−13.5%)

3.2. Formation energy

As discussed in section 2.2, the formation energy E_{form} is a by-product of the lattice parameter calculation. Figure 2 summarizes values of E_{form} based on four IAPs. For Nb-W and Ta-W alloys, all the methods predict the same trend in E_{form}. As the amount of W in the alloy increases, E_{form} increases till the W percentage reaches 60%. However, the absolute values of the E_{form} anticipated by the different IAPs vary to some extent. For example, E_{form} predicted by EAM is lower than that predicted by the other methods, while MTP predicts the highest E_{form}. For Mo-W alloys, the slope of the decrease is steeper for MTP and tabGAP compared to EAM and SNAP. Additionally, values of E_{form} based on MTP and tabGAP are more negative compared to EAM and SNAP for all W percentages. There is a significant difference between the E_{form} values predicted by the different IAPs. For example, at 0.1 W percentage, E_{form} predicted by MTP and tabGAP are about three times more negative than the values predicted by EAM and SNAP. The plots also show that the uncertainties or errors associated with each method are relatively small. Overall, the plots suggest that the different computational methods agree well with each other in predicting the formation energy of the alloys.

3.3. Elastic constants

In figure 3, the elastic constants predicted by the four IAPs exhibit a similar overall trend, but with notable discrepancies among their absolute values. Specifically, for C_{11}, tabGAP predicts the most accurate value for the Mo-W alloys, Mo, Nb, and Ta, when compared with DFT values. For all pure metals, the EAM potentials yield the second-best values of C_{11} with respect to DFT, after tabGAP. In the meantime, MTP-based values show the highest differences with respect to DFT data in all three sets of alloys.

Regarding C_{12}, EAM shows the least difference when compared with DFT data, followed by SNAP potentials, while MTPs predict the least accurate values. For C_{44}, with respect to DFT, SNAP is shown to be the best IAP, followed by EAM, while tabGAPs fair the worst. Overall, there is no single IAP that is the best in predicting all three elastic constants.

Based on C_{11}, C_{12}, and C_{44}, we then derive the bulk modulus B_{mod} in all random binaries and pure metals, following is the relationship: [63]

$$B_{mod} = (C_{11} + 2C_{12})/3 \tag{13}$$

Results in figure 4 show that, for Ta-W, Nb-W alloys, B_{mod} increases gradually with an increasing W percentage, demonstrating the most uniform behavior among the three alloys, across all the IAP. In contrast, for Mo-W alloys, the bulk modulus (B_{mod}) predictions exhibit the most variability across different IAPs. There is an observable overall trend of the B_{mod} increasing when W increased. From table 1 we can see the difference in the bulk moduli predicted from all four potentials with respect to DFT values for $Mo_{0.5}W_{0.5}$. Compared with the

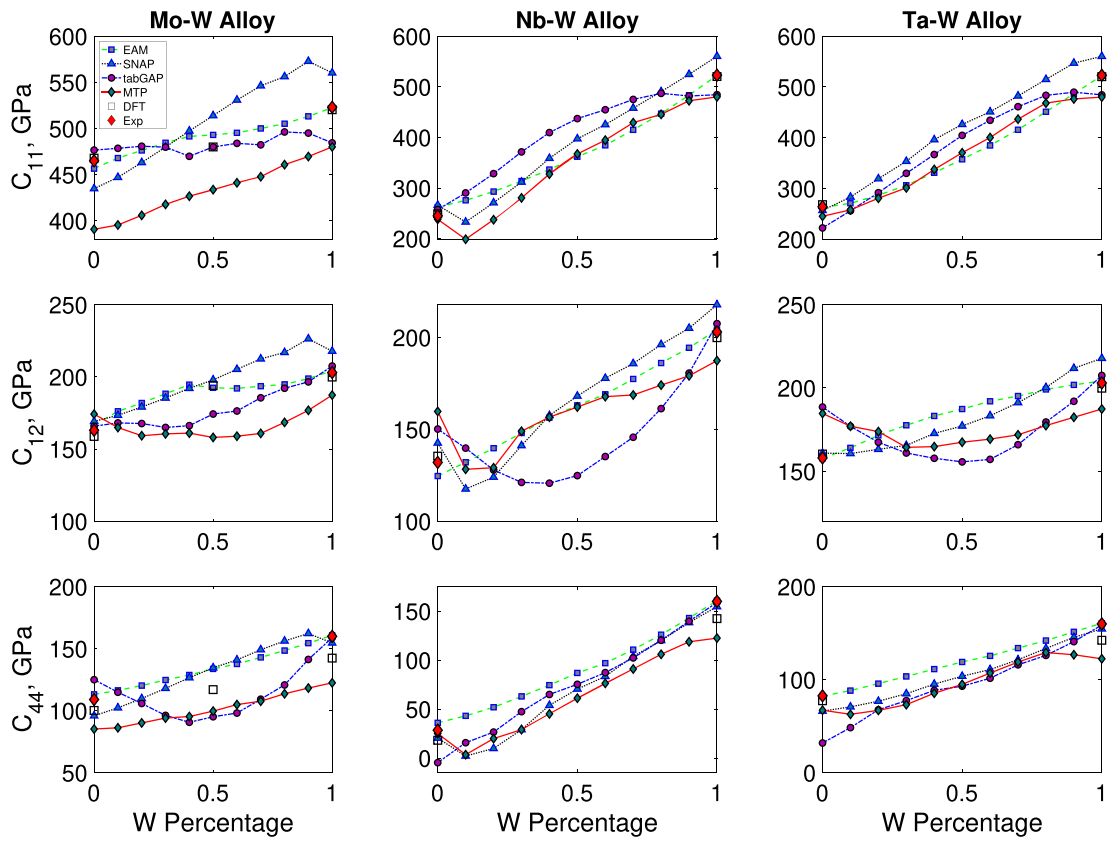

Figure 3. Three independent elastic constants based on different IAPs in three alloys are plotted with respect to the percentage of W in the alloy. The experimental and DFT data from [62, 67].

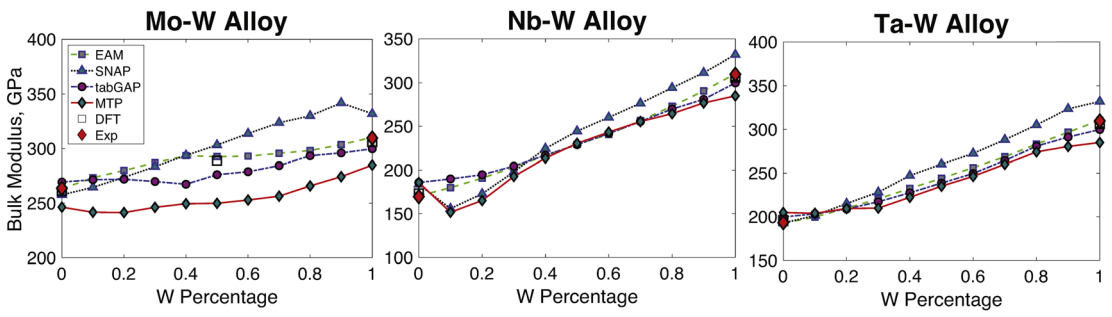

Figure 4. Bulk moduli based on different IAPs in three alloys are plotted with respect to the percentage of W in the alloy. The DFT and experimental values are taken from [62, 67].

DFT values, EAM potentials produced the closest, where MTPs produced the values with the biggest difference when predicting the B_{mod}.

Table 3 presents the determined elastic constants for pure metals from all four potentials, which are then compared to values obtained from both DFT and experimental measurements. None of the potentials consistently produce more accurate results across all materials and elastic constants. As tabGAP was not specifically calibrated to model elastic constants, it yields results that display greater variance when compared to the DFT values. However, the EAM method appears to provide a relatively close estimate to the experimental values for most materials, making it potentially the most accurate overall, while tabGAP and MTP show more significant discrepancies.

3.4. Peierls stress

The characteristics of a dislocation in a metal are closely related to the Peierls stress, which is the resolved shear stress required to move a dislocation within its glide plane [64]. Peierls stress and Peierls barrier are the two

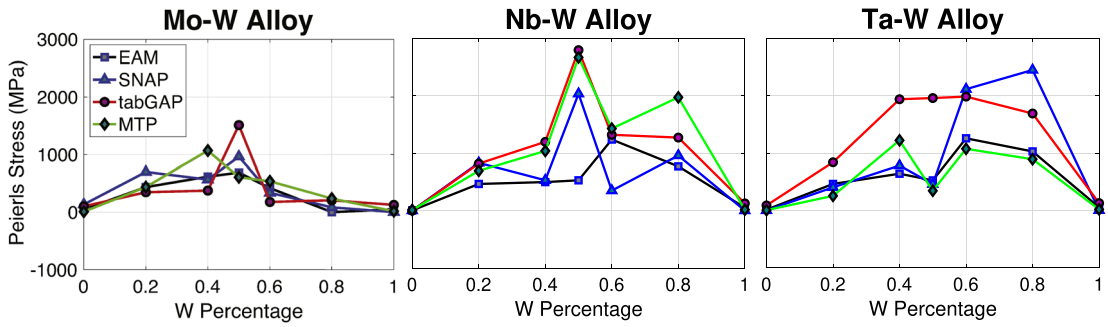

Figure 5. Peierls stress based on different IAPs in three alloys are plotted with respect to the percentage of W in the alloy.

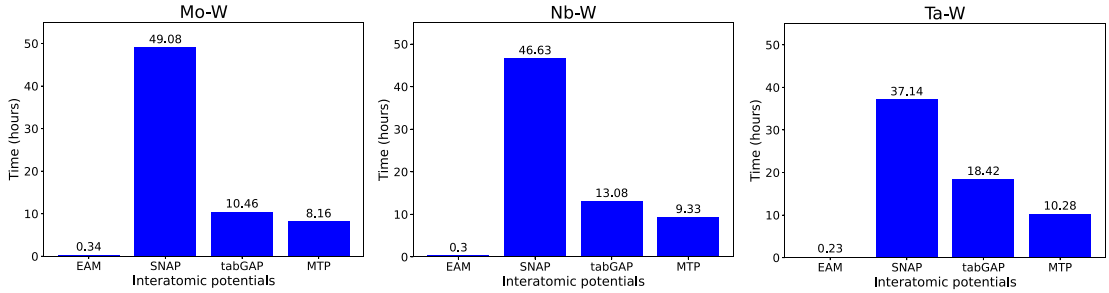

Figure 6. Computational time consumed by different IAPs, when calculating the Peierls stress of an edge dislocation in the $Mo_{0.5}W_{0.5}$, $Nb_{0.5}W_{0.5}$, and $Ta_{0.5}W_{0.5}$ alloy.

primary indicators of the lattice's resistance to dislocation motion. Both have a connection to the mechanism of the dislocation transferring from a Peierls valley to a nearby valley [65]. Regarding the study's emphasis on edge dislocations, the rationale is twofold. Primarily, there is relatively little research focused on edge dislocations compared to screw dislocations. Additionally, the complexity of calculating the Peierls stress for screw dislocations, largely due to their tendency to cross slip to different planes, underscore the relevance of focusing on edge dislocations in this study [59, 66].

Figure 5 illustrates the Peierls stress of an edge dislocation in Mo-W, Nb-W, and Ta-W alloys predicted by the four IAPs. Among different IAPs, the same alloy is characterized by the same initial structure (except for the different lattice parameters), which is essential to ensure the comparability of the results. It is found that the trends of the Peierls stress are largely consistent for different IAPs, albeit with some exceptions. To our best knowledge, there have not been any previous reports of either *ab initio* calculations or measured values for the Peierls stresses of edge dislocations in any of the metals under consideration [47]. So taking the MTP values as references, some insights can be gained in terms of other IAPs. It's important to note that the choice of MTP does not imply its superiority, MTP only serves as a common baseline against which other models can be compared. Specifically, the EAM potentials have the smallest deviation from MTP in Mo-W alloys, while tabGAP shows the largest deviation. Conversely, tabGAP shows the least deviation in Nb-W alloys, while EAM potentials exhibit the largest deviation. For Ta-W alloys, the EAM potentials demonstrate the least variance, while tagGAP is the largest.

3.5. Efficiency

In evaluating the efficiency of the IAPs, the same computational resources were employed to execute identical calculations. The LAMMPS version that was used for all calculations was the one released on January 7th, 2022. For the simulations, three nodes, each equipped with 32 cores, were used. Here, the Peierls stress simulations in $Mo_{0.5}W_{0.5}$, $Nb_{0.5}W_{0.5}$, and $Ta_{0.5}W_{0.5}$ are chosen for assessing the computational efficiency. From figure 6, it could be said that SNAP requires the greatest amount of computational time, while the EAM potential demonstrates the highest level of computational efficiency. Among the ML-IAPs, MTP exhibits an average around five-fold increase in computational speed compared to SNAP when using identical computational resources. The analysis can aid in selecting the right IAPs for specific computations.

Table 3. Comparison of elastic constants (C_{11}, C_{12}, and C_{44} in GPa) for Mo, Nb, Ta, and W obtained from different methods: Experiment (Exp) [68–70], DFT [8], SNAP, tabGAP, MTP, and EAM.

	Mo			Nb			Ta			W		
	C_{11}	C_{12}	C_{44}	C_{11}	C_{12}	C_{44}	C_{11}	C_{12}	C_{44}	C_{11}	C_{12}	C_{44}
Exp	479	165	108	249	135	19	266	158	87	533	205	163
DFT	472	158	106	247	135	29	264	161	74	511	200	142
SNAP	434	169	95	266	142	20	256	160	66	560	217	154
tabGAP	476	165	125	257	150	−4	222	189	48	484	207	159
MTP	390	174	85	238	159	24	245	184	67	480	187	122
EAM	456	166	113	262	124	36	262	157	82	522	204	160

4. Conclusion

In this study, MS simulations are performed to calculate basic structural parameters and Peierls stress of an edge dislocation in Mo-W, Nb-W, and Ta-W alloys and their corresponding pure metals: Mo, Nb, Ta, and W. Nine combinations of each set of binary alloy are investigated. The simulations utilized four IAPs, including the EAM potential, which is a non-ML-IAP, and three ML-IAPs: SNAP, tabGAP, and MTP. Results show discrepancies among the values obtained from the four IAPs. In terms of the lattice parameter, as compared with DFT data, MTP differs the least while EAM the most. All four IAPs predict that the lattice parameter increases with an increasing W concentration, with the exception of the Mo-W alloys, which showed the opposite trend. In terms of the formation energy, all four IAPs lead to similar results. The errors introduced by the fitting procedure are relatively small compared to the magnitude of the formation energy itself.

In addition to lattice parameters and formation energies, the accurate prediction of elastic constants is also crucial for understanding alloys, and this study provides important insights. It is found that tabGAP is particularly effective in predicting C_{11} and C_{12} for both pure metals and Mo-W alloys, as its predictions are the closest to the corresponding DFT values. In contrast, SNAP is found to be the most accurate in predicting the C_{44} values for the pure metals, whereas MTP is the most accurate for the binary alloys. In predicting the Peierls stress of an edge dislocation, with respect to the MTP-based values, SNAPs are found to provide the closest values, followed by the EAM potentials and tabGAPs.

This study also compares the efficiency of the four IAPs. Results show that the EAM potential is the most efficient, requiring the least amount of computational time, followed by MTP, then tabGAP, and SNAP being the slowest when calculating the Peierls stress. Taken together, our study highlights the trade-off between computational efficiency and accuracy in developing or choosing IAPs in future computational materials science research. The specific focus on lattice constants, elastic constants, formation energy, and Peierls stress in this study was intentional, offering a basic but crucial insight into the materials' behavior. While this paper represents an initial step, the findings aim to guide more comprehensive research in the future. It is essential to highlight that the use of different Machine Learning-based potentials in atomistic simulations can yield significant variations, even in basic parameters.

Acknowledgments

This work used Bridges-2 at the Pittsburgh Supercomputing Center through allocation MAT220034 from the Advanced Cyberinfrastructure Coordination Ecosystem: Services & Support (ACCESS) program, which is supported by National Science Foundation grants #2138259, #2138286, #2138307, #2137603, and #2138296. The support and resources from the Center for High Performance Computing at the University of Utah are gratefully acknowledged. AAM and YS thank the start-up funds provided by the Utah State University.

Data availability statement

All data that support the findings of this study are included within the article (and any supplementary files).

ORCID iDs

Shuozhi Xu https://orcid.org/0000-0003-0121-9445
Yanqing Su https://orcid.org/0000-0003-0790-5905

References

[1] Kobayashi E, Matsumoto S, Doi H, Yoneyama T and Hamanaka H 1995 Mechanical properties of the binary titanium-zirconium alloys and their potential for biomedical materials *Journal of Biomedical Materials Research* **29** 943–50

[2] Romaner L, Ambrosch-Draxl C and Pippan R 2010 Effect of rhenium on the dislocation core structure in tungsten *Phys. Rev. Lett.* **104** 195503

[3] Wang L L and Johnson D D 2009 Predicted trends of core-shell preferences for 132 late transition-metal binary-alloy nanoparticles JACS **131** 14023–9

[4] Tang Z, Niu J, Huang H, Zhang H, Pei J, Ou J and Yuan G 2017 Potential biodegradable Zn-Cu binary alloys developed for cardiovascular implant applications *J. Mech. Behav. Biomed. Mater.* **72** 182–91

[5] Senkov O N, Wilks G, Scott J and Miracle D B 2011 Mechanical properties of $Nb_{25}Mo_{25}Ta_{25}W_{25}$ and $V_{20}Nb_{20}Mo_{20}Ta_{20}W_{20}$ refractory high entropy alloys *Intermetallics* **19** 698–706

[6] Feng X, Zhang J, Xia Z, Fu W, Wu K, Liu G and Sun J 2018 Stable nanocrystalline NbMoTaW high entropy alloy thin films with excellent mechanical and electrical properties *Mater. Lett.* **210** 84–7

[7] Juan C C, Tsai M H, Tsai C W, Lin C M, Wang W R, Yang C C, Chen S K, Lin S J and Yeh J W 2015 Enhanced mechanical properties of HfMoTaTiZr and HfMoNbTaTiZr refractory high-entropy alloys *Intermetallics* **62** 76–83

[8] Li X G, Chen C, Zheng H, Zuo Y and Ong S P 2020 Complex strengthening mechanisms in the NbMoTaW multi-principal element alloy *npj Comput. Mater.* **6** 70

[9] Gludovatz B, Hohenwarter A, Catoor D, Chang E H, George E P and Ritchie R O 2014 A fracture-resistant high-entropy alloy for cryogenic applications *Science* **345** 1153–8

[10] Gludovatz B, Hohenwarter A, Thurston K V, Bei H, Wu Z, George E P and Ritchie R O 2016 Exceptional damage-tolerance of a medium-entropy alloy CrCoNi at cryogenic temperatures *Nat. Commun.* **7** 10602

[11] Senkov O, Wilks G, Miracle D, Chuang C and Liaw P 2010 Refractory high-entropy alloys *Intermetallics* **18** 1758–65

[12] Senkov O N, Miracle D B, Chaput K J and Couzinie J P 2018 Development and exploration of refractory high entropy alloysA review *J. Mater. Res.* **33** 3092–128

[13] Xu S, Jian W R and Beyerlein I J 2022 Ideal simple shear strengths of two HfNbTaTi-based quinary refractory multi-principal element alloys *APL Mater.* **10** 111107

[14] Xu S, Al Mamun A, Mu S and Su Y 2023 Uniaxial deformation of nanowires in 16 refractory multi-principal element alloys *J. Alloys Compd.* **959** 170556

[15] Xu S, Chavoshi S Z and Su Y 2022 On calculations of basic structural parameters in multi-principal element alloys using small atomistic models *Comput. Mater. Sci.* **202** 110942

[16] Natarajan A R, Dolin P and Van der Ven A 2020 Crystallography, thermodynamics and phase transitions in refractory binary alloys *Acta Mater.* **200** 171–86

[17] Beyerlein I J, Xu S, Llorca J, El-Awady J A, Mianroodi J R and Svendsen B 2019 Alloy design for mechanical properties: conquering the length scales *MRS Bull.* **44** 257–65

[18] Li X G, Hu C, Chen C, Deng Z, Luo J and Ong S P 2018 Quantum-accurate spectral neighbor analysis potential models for Ni-Mo binary alloys and fcc metals *Phys. Rev.* B **98** 094104

[19] Miracle D B and Senkov O N 2017 A critical review of high entropy alloys and related concepts *Acta Mater.* **122** 448–511

[20] Xu S, Kulathuvayal A S, Xiong L and Su Y 2022 Effects of ferromagnetism in ab initio calculations of basic structural parameters of Fe-A (A=Mo, Nb, Ta, V, or W) random binary alloys *Eur. Phys. J.* B **95** 167

[21] Li X G, Xu S, Zhang Q, Liu S and Shuai J 2023 Complex strengthening mechanisms in nanocrystalline Ni-Mo alloys revealed by a machine-learning interatomic potential *J. Alloys Compd.* **952** 169964

[22] Ababkov V and Morgunova N 1973 Mechanical properties of Mo-W alloys *Met. Sci. Heat Treat.* **15** 376–378

[23] Wang S, Wu Z, Xie M, Si D, Li L, Chen C, Zhang Z and Wu Y 2020 The effect of tungsten content on the rolling texture and microstructure of Ta-W alloys *Mater. Charact.* **159** 110067

[24] Tawancy H M, Herchenroeder R B and Asphahani A I 1983 High-performance Ni-Cr-Mo-W alloys *JOM* **35** 37–43

[25] Ma C, Li J, Tan Y, Tanaka R and Hanada S 2004 Microstructure and mechanical properties of Nb/Nb_5Si_3 in situ composites in Nb-Mo-Si and Nb-W-Si systems *Materials Science and Engineering: A* **386** 375–83

[26] Nogami S, Hasegawa A, Fukuda M, Rieth M, Reiser J and Pintsuk G 2021 Mechanical properties of tungsten: recent research on modified tungsten materials in Japan *J. Nucl. Mater.* **543** 152506

[27] Wurster S *et al* 2013 Recent progress in R&D on tungsten alloys for divertor structural and plasma facing materials *J. Nucl. Mater.* **442** S181–9

[28] Gumbsch P 2003 Brittle fracture and the brittle-to-ductile transition of tungsten *J. Nucl. Mater.* **323** 304–12

[29] Rau R, Moteff J and Ladd R 1967 Comparison of microstructure with mechanical properties of irradiated tungsten *J. Nucl. Mater.* **24** 164–73

[30] Wakai E *et al* 2022 Development of innovative materials and measurement systems used for radiation environment *Research & Development in Material Science* **16** 1859–67

[31] Thompson A P *et al* 2022 LAMMPS - a flexible simulation tool for particle-based materials modeling at the atomic, meso, and continuum scales *Comput. Phys. Comm.* **271** 108171

[32] Kresse G and Furthmüller J 1996 Efficient iterative schemes for ab initio total-energy calculations using a plane-wave basis set *Phys. Rev.* B **54** 11169–86

[33] Kohn W and Sham L J 1965 Self-consistent equations including exchange and correlation effects *Phys. Rev.* **140** A1133

[34] Zhang I Y, Xu X, Jung Y and Goddard W A 2011 A fast doubly hybrid density functional method close to chemical accuracy using a local opposite spin ansatz *Proc. Natl Acad. Sci.* **108** 19896–900

[35] Ji H, Shao Y, Goddard W A and Jung Y 2013 Analytic derivatives of quartic-scaling doubly hybrid XYGJ-OS functional: Theory, implementation, and benchmark comparison with M06-2X and MP2 geometries for nonbonded complexes *J. Chem. Theory Comput.* **9** 1971–6

[36] Van Duin A C, Dasgupta S, Lorant F and Goddard W A 2001 ReaxFF: a reactive force field for hydrocarbons *The Journal of Physical Chemistry* A **105** 9396–409

[37] Mayo S L, Olafson B D and Goddard W A 1990 Dreiding: a generic force field for molecular simulations *J. Phys. Chem.* **94** 8897–909

[38] Daw M S and Baskes M I 1984 Embedded-atom method: derivation and application to impurities, surfaces, and other defects in metals *Phys. Rev.* B **29** 6443

[39] Szelestey P, Patriarca M, Perondi L and Kaski K 2002 Modified EAM potentials for modelling stacking-fault behavior in Cu, Al, Au, and Ni *Int. J. Mod. Phys. B* **16** 2823–35
[40] Zhou X W, Johnson R A and Wadley H N G 2004 Misfit-energy-increasing dislocations in vapor-deposited CoFe/NiFe multilayers *Phys. Rev.* B **69** 144113
[41] Mishin Y 2021 Machine-learning interatomic potentials for materials science *Acta Mater.* **214** 116980
[42] Behler J Perspective 2016 Machine learning potentials for atomistic simulations *J. Chem. Phys.* **145** 170901
[43] Blank T B, Brown S D, Calhoun A W and Doren D J 1995 Neural network models of potential energy surfaces *J. Chem. Phys.* **103** 4129–37
[44] Bartók A P, Payne M C, Kondor R and Csányi G 2010 Gaussian approximation potentials: the accuracy of quantum mechanics, without the electrons *Phys. Rev. Lett.* **104** 136403
[45] Thompson A P, Swiler L P, Trott C R, Foiles S M and Tucker G J 2015 Spectral neighbor analysis method for automated generation of quantum-accurate interatomic potentials *J. Comput. Phys.* **285** 316–30
[46] Shapeev A V 2016 Moment tensor potentials: a class of systematically improvable interatomic potentials *Multiscale Modeling & Simulation* **14** 1153–73
[47] Wang X, Xu S, Jian W R, Li X G, Su Y and Beyerlein I J 2021 Generalized stacking fault energies and Peierls stresses in refractory body-centered cubic metals from machine learning-based interatomic potentials *Comput. Mater. Sci.* **192** 110364
[48] Tian F, Wang Y and Vitos L 2017 Impact of aluminum doping on the thermo-physical properties of refractory medium-entropy alloys *J. Appl. Phys.* **121** 015105
[49] Byggmästar J, Nordlund K and Djurabekova F 2021 Machine-learned interatomic potential for Mo-Nb-Ta-V-W (2+3-body tabGAP) (https://doi.org/10.23729/1b845398-5291-4447-b417-1345acdd2eae)
[50] Yin S, Zuo Y, Abu-Odeh A, Zheng H, Li X G, Ding J, Ong S P, Asta M and Ritchie R O 2021 Atomistic simulations of dislocation mobility in refractory high-entropy alloys and the effect of chemical short-range order *Nat. Commun.* **12** 4873
[51] Daw M S, Foiles S M and Baskes M I 1993 The embedded-atom method: a review of theory and applications *Materials Science Reports* **9** 251–310
[52] Stott M and Zaremba E 1980 Quasiatoms: an approach to atoms in nonuniform electronic systems *Phys. Rev.* B **22** 1564
[53] Zuo Y *et al* 2020 Performance and cost assessment of machine learning interatomic potentials *The Journal of Physical Chemistry* A **124** 731–45
[54] Byggmästar J, Hamedani A, Nordlund K and Djurabekova F 2019 Machine-learning interatomic potential for radiation damage and defects in tungsten *Phys. Rev.* B **100** 144105
[55] Byggmästar J, Nordlund K and Djurabekova F 2021 Modeling refractory high-entropy alloys with efficient machine-learned interatomic potentials: defects and segregation *Phys. Rev.* B **104** 104101
[56] Ashcroft N W and Mermin N D 2022 *Solid State Physics.* (Cengage Learning)
[57] Xu S, Hwang E, Jian W R, Su Y and Beyerlein I J 2020 Atomistic calculations of the generalized stacking fault energies in two refractory multi-principal element alloys *Intermetallics* **124** 106844
[58] Osetsky Y N and Bacon D J 2003 An atomic-level model for studying the dynamics of edge dislocations in metals *Modell. Simul. Mater. Sci. Eng.* **11** 427
[59] Xu S, Su Y, Jian W R and Beyerlein I J 2021 Local slip resistances in equal-molar MoNbTi multi-principal element alloy *Acta Mater.* **202** 68–79
[60] Bitzek E, Koskinen P, Gähler F, Moseler M and Gumbsch P 2006 Structural relaxation made simple *Phys. Rev. Lett.* **97** 170201
[61] Stukowski A 2010 Visualization and analysis of atomistic simulation data with OVITO–the Open Visualization Tool *Modell. Simul. Mater. Sci. Eng.* **18** 015012
[62] Nikoulis G, Byggmästar J, Kioseoglou J, Nordlund K and Djurabekova F 2021 Machine-learning interatomic potential for W-Mo alloys *J. Phys. Condens. Matter* **33** 315403
[63] Ashby M F and Jones D R H 2011 *Engineering Materials 1: An Introduction to Properties, Applications and Design* vol 1 (Elsevier)
[64] Soboyejo W 2002 *Mechanical Properties of Engineered Materials* (CRC Press) (https://doi.org/10.1201/9780203910399)
[65] Ganchenkova M and Nieminen R M 2015 Mechanical properties of silicon microstructures *Handbook of Silicon Based MEMS Materials and Technologies* (Elsevier) pp 263–303
[66] Hale L M, Zimmerman J A and Weinberger C R 2014 Simulations of bcc tantalum screw dislocations: Why classical inter-atomic potentials predict {112} slip *Comput. Mater. Sci.* **90** 106–15
[67] Xu S, Su Y, Smith L T and Beyerlein I J 2020 Frank-read source operation in six body-centered cubic refractory metals *J. Mech. Phys. Solids* **141** 104017
[68] Trivisonno J, Vatanayon S, Wilt M, Washick J and Reifenberger R 1973 Temperature dependence of the elastic constants of niobium and lead in the normal and superconducting states *J. Low Temp. Phys.* **12** 153–69
[69] Simmons G and Wang H 1971 *Single Crystal Elastic Constants and Calculated Aggregate Properties: A Handbook* (MIT Press)
[70] Featherston F H and Neighbours J 1963 Elastic constants of tantalum, tungsten, and molybdenum *Phys. Rev.* **130** 1324